AIP | Journal of Applied Physics

High-frequency thermal-electrical cycles for pyroelectric energy conversion

Bikram Bhatia, Anoop R. Damodaran, Hanna Cho, Lane W. Martin, and William P. King

Citation: Journal of Applied Physics **116**, 194509 (2014); doi: 10.1063/1.4901993
View online: http://dx.doi.org/10.1063/1.4901993
View Table of Contents: http://scitation.aip.org/content/aip/journal/jap/116/19?ver=pdfcov
Published by the AIP Publishing

High-frequency thermal-electrical cycles for pyroelectric energy conversion

Bikram Bhatia,[1] Anoop R. Damodaran,[2] Hanna Cho,[3] Lane W. Martin,[2,4] and William P. King[1,2,a)]

[1]*Department of Mechanical Science and Engineering, University of Illinois Urbana-Champaign, Urbana, Illinois 61801, USA*
[2]*Department of Materials Science and Engineering and Materials Research Laboratory, University of Illinois Urbana-Champaign, Urbana, Illinois 61801, USA*
[3]*Department of Mechanical Engineering, Texas Tech University, Lubbock, Texas 79409, USA*
[4]*Department of Materials Science and Engineering, University of California, Berkeley, California 94720, USA*

(Received 27 June 2014; accepted 5 November 2014; published online 21 November 2014)

We report thermal to electrical energy conversion from a 150 nm thick $BaTiO_3$ film using pyroelectric cycles at 1 kHz. A microfabricated platform enables temperature and electric field control with temporal resolution near 1 μs. The rapid electric field changes as high as 11×10^5 kV/cm-s, and temperature change rates as high as 6×10^5 K/s allow exploration of pyroelectric cycles in a previously unexplored operating regime. We investigated the effect of phase difference between electric field and temperature cycles, and electric field and temperature change rates on the electrical energy generated from thermal-electrical cycles based on the pyroelectric Ericsson cycle. Complete thermodynamic cycles are possible up to the highest cycle rates tested here, and the energy density varies significantly with phase shifts between temperature and electric field waveforms. This work could facilitate the design and operation of pyroelectric cycles at high cycle rates, and aid in the design of new pyroelectric systems. © *2014 AIP Publishing LLC*.
[http://dx.doi.org/10.1063/1.4901993]

I. INTRODUCTION

Waste heat accounts for more than half the energy produced in the world.[1] A significant fraction of this rejected energy is at low temperature which is difficult to harvest efficiently. Thermoelectric devices that convert spatial temperature variations into electrical energy are one solution to this problem.[2] However, the relatively low efficiencies of thermoelectric materials, along with constraints on operating environments have prevented widespread adoption.[3] Other solutions include heat exchangers that convert thermal energy into useful work using a liquid or gas based thermodynamic cycle.[4] The moving parts and fluid flows required in these systems, however, cannot be easily scaled to small sizes or rapid cycle rates.

Pyroelectric energy conversion utilizes the temperature dependence of electric displacement of polar materials to convert temperature fluctuations into electrical energy.[5–8] Initial first principle studies predicted electricity generation from heat using pyroelectric materials to be unfeasible due to energy conversion efficiencies less than 1%.[9,10] More recent studies have, however, found energy densities up to 1 J/cm^3 and efficiencies as high as 5.4% of the Carnot limit using thermodynamic cycles that utilize temperature as well as electric field dependence of the electric displacement of pyroelectric materials.[11,12] The four-step pyroelectric Ericsson cycle is one such thermodynamic cycle that consists of two isothermal and two isoelectric processes.[12,13] Pyroelectric energy conversion using such thermal-electrical cycles can be particularly attractive for systems with temperature fluctuations, such as internal combustion engines and power electronics that produce low-quality, low-temperature waste heat.[14,15]

Investigation of pyroelectric energy conversion using thermal-electrical cycles requires a setup that can simultaneously vary the temperature and electric field across the pyroelectric material in time. Published research on pyroelectric energy conversion has commonly used oil baths or pumping fluid to generate temperature oscillations in bulk samples, typically at frequencies less than 1 Hz.[11,13,16–19] Other methods of temperature control used thermal contact with hot and cold metal blocks or switchable liquid interfaces.[20,21] Desired electric fields required application of voltages as high as a few kV across the thick samples which are impractical for most applications.[17,22] Use of bulk samples with large thermal mass and coarse thermal and electrical control limited the investigation of pyroelectric energy conversion to slow changes in temperature and electric field. While some published studies have investigated the effect of temperature oscillation amplitude, electric field range, and cycle frequency on pyroelectric energy conversion, very few have examined the effect of temporal variations in temperature and applied electric field.[11,23,24]

This paper presents an analysis of the transient thermal and electrical operation of pyroelectric energy conversion cycles with the goal of maximizing the output electrical energy density. We developed a microfabricated platform consisting of a 150 nm thick $BaTiO_3$ film that allows simultaneous, high-frequency thermal and electrical cycling. The device enables investigation of the energy conversion process in the pyroelectric film in response to arbitrary variations in temperature and electric field with microsecond

a)Electronic mail: wpk@illinois.edu

temporal control. We studied the effect of phase shifts between heating and electric field at a cycle frequency of 1 kHz, electric field change rates between 1.42×10^5 kV/cm-s and 11.33×10^5 kV/cm-s, and temperature change rates around 6×10^5 K/s on the pyroelectric energy conversion process. Thermal-electrical cycles obtained using different temperature and electric field profiles are compared with the pyroelectric Ericsson cycle.

II. PYROELECTRIC ENERGY CONVERSION TEST PLATFORM

Figure 1 shows the construction and thermal-electrical operation of the pyroelectric energy conversion test platform.[24] The device consists of a $BaTiO_3$ thin-film capacitor with electrical access to top and bottom electrodes. A gold strip placed above the pyroelectric capacitor serves as the resistive heater. A high resistivity SiO_2 layer, sandwiched between the top electrode and heater strip, electrically insulates the pyroelectric film and minimizes interference from the heating voltage.

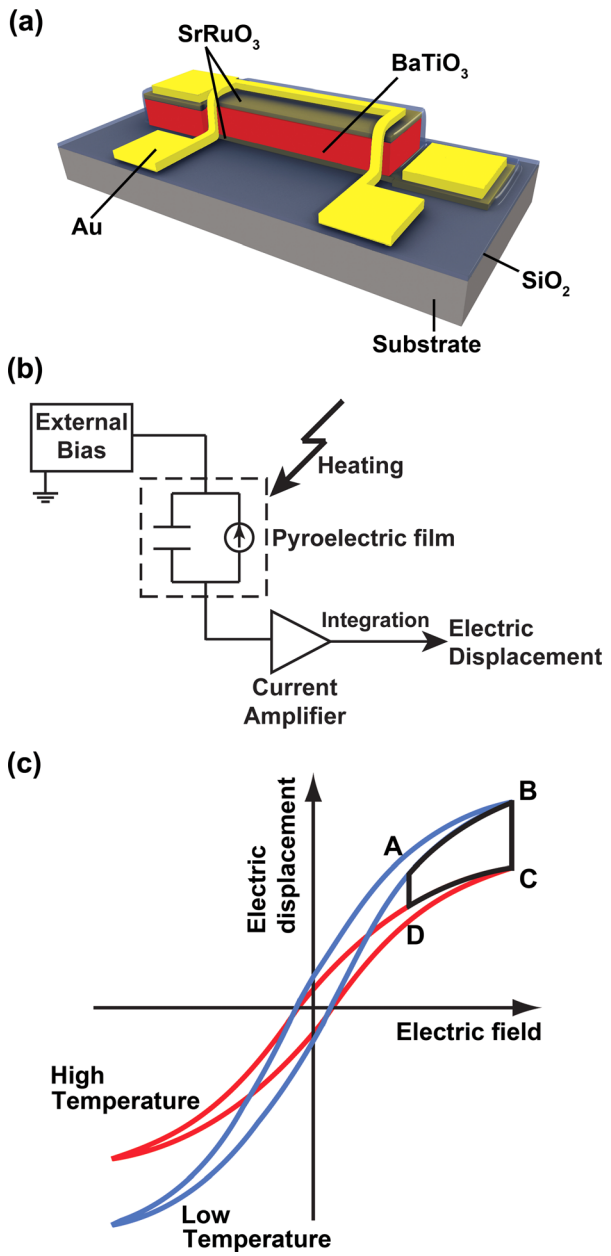

FIG. 1. (a) Schematic of the microfabricated device consisting of a 150 nm thick $BaTiO_3$ film and (b) the setup used to implement pyroelectric thermal-electrical cycles. (c) Illustration of the four-step pyroelectric Ericsson cycle on an electric displacement versus electric field plot superimposed on *D-E* loops shown at two temperatures.

The pyroelectric film was integrated in the test platform using standard microfabrication techniques. Figure 1(a) shows the schematic of the device. The substrate was 5 mm × 5 mm × 0.5 mm $GdScO_3$ (110). The films were 40 nm $SrRuO_3$ and 150 nm $BaTiO_3$, and were deposited using pulsed laser deposition.[25] The choice of a $GdScO_3$ single crystal substrate was based on its excellent structural, chemical, and thermal compatibility with $BaTiO_3$.[26] (See supplementary material for details on film deposition and characterization.)[27] These two layers were then selectively etched by ion milling using a hard-baked photoresist mask to define the bottom electrode and active material of the ferroelectric capacitor. Next, a sacrificial MgO mask was deposited using photoresist lift-off and e-beam evaporation to define the top electrode.[28] The 80 nm thick top $SrRuO_3$ electrode was fabricated using pulsed laser deposition followed by an MgO lift-off step in phosphoric acid. Then, a 150 nm thick layer of SiO_2 was deposited over the 500 μm × 20 μm ferroelectric capacitor using plasma enhanced chemical vapor deposition. Freon reactive ion etching of the SiO_2 layer and manual scratching of the $BaTiO_3$ layer were used to access the top and bottom electrodes of the capacitor. Finally, we fabricated the 10 μm wide, 440 μm long heater strip and contact pads over the SiO_2 layer using sputter deposition of 10 nm Cr/100 nm Au followed by a photoresist lift-off process.

Figure 1(b) shows the setup used to monitor the pyroelectric cycles. The $BaTiO_3$ film is represented as a dielectric capacitor in parallel with a temperature-change-rate dependent current source. The electric displacement (D) of the pyroelectric film varies with changes in external electric field (E) as well as temperature (T), which causes an electric current to flow in the external circuit. The pyroelectric film electric displacement change was found by numerically integrating the electric current measured from the bottom $SrRuO_3$ electrode using a current-to-voltage converter as in the virtual ground method.[29] The top $SrRuO_3$ electrode was either grounded or maintained at a fixed voltage to decouple the heating circuit from the current measurement circuit.

Pyroelectric energy conversion cycles rely upon thermal as well as electrical response of the electric displacement. Figure 1(c) shows an illustration of the pyroelectric Ericsson cycle A-B-C-D alongside the corresponding isothermal *D-E* loops at the maximum and minimum temperatures. A typical pyroelectric Ericsson cycle comprises two isothermal processes, A→B and C→D, and two isoelectric processes, B→C and D→A. Starting from A, the out-of-plane electric field is first increased at low temperature, increasing the electric displacement. Then, the temperature is increased while the electric field is held constant at a high value, resulting in a decrease in the electric displacement. Next, the electric field is reduced to its low value at high temperature, again

decreasing the electric displacement. Finally, the clockwise cycle is completed by lowering the temperature to its original value at a constant low electric field. The area of the cycle A-B-C-D represents the total electrical energy density output from the pyroelectric cycle.

A. Electrical characterization

The field-dependence of the $BaTiO_3$ film electric displacement was characterized using room temperature displacement-electric field (*D-E*) loops shown in Figure 2(a).[27] A 1 kHz triangular voltage waveform was applied to the top $SrRuO_3$ electrode. The resulting current was measured from the bottom $SrRuO_3$ electrode and the film electric displacement change was determined using the virtual ground method.[29] The Curie temperature of the ferroelectric film is about 400 °C (see supplementary material for the temperature dependence of the dielectric constant[27]). All measurements were performed below the Curie temperature, where the film electric displacement decreases with increase in temperature as shown in Figure 1(c).

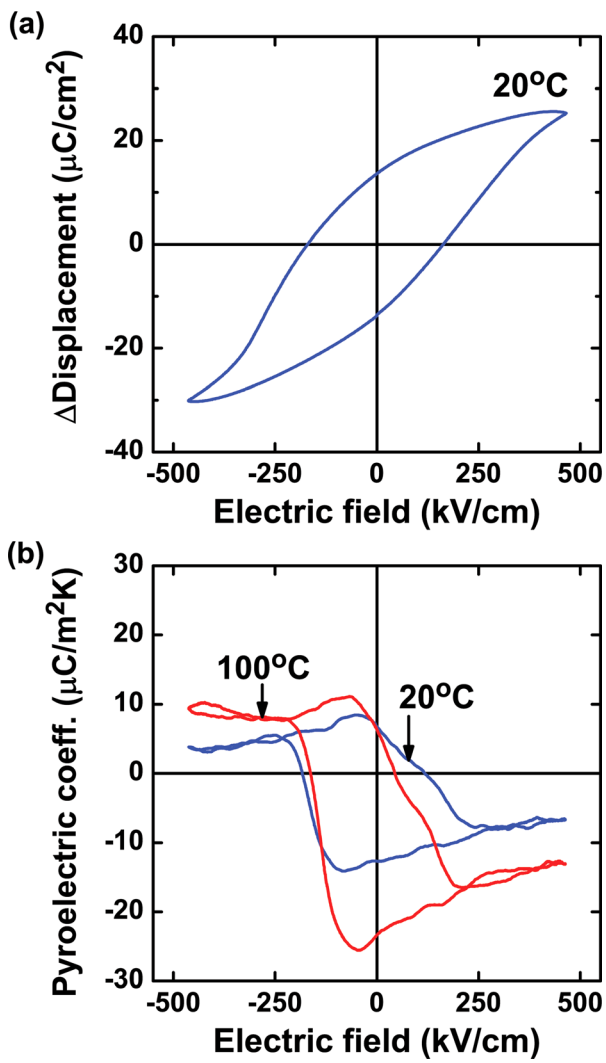

FIG. 2. (a) Room temperature displacement-electric field loops measured at 1 kHz excitation frequency and (b) pyroelectric loops measured using the $BaTiO_3$ device at 2 kHz heating frequency and at temperatures 20 °C and 100 °C.

We characterized the temperature dependence of ferroelectric electric displacement by measuring the pyroelectric current from the device generated due to sinusoidal heating of the thin film.[30] Figure 2(b) shows the pyroelectric coefficient of the $BaTiO_3$ film measured as a function of out-of-plane electric field using a lock-in amplifier based 2ω method.[30] A sinusoidal voltage at 1 kHz applied to the heater strip causes a temperature oscillation in the $BaTiO_3$ film at 2 kHz. The temperature fluctuation generates pyroelectric current which was measured from the bottom electrode. The voltage on the top electrode was simultaneously varied with the heating bias at 0.1 Hz to obtain the field-dependence of the pyroelectric response (see supplementary material for details[27]). Measurements were performed at constant background temperatures of 20 and 100 °C, controlled using a bulk heating stage. The pyroelectric coefficient was calculated by dividing the pyroelectric current, measured at the temperature oscillation frequency, with the capacitor area and the calculated time rate of change of temperature. The measured pyroelectric coefficient shown in Figure 2(b) increases as the background temperature increases from 20 to 100 °C, as is expected for a ferroelectric below the Curie temperature.

B. Pyroelectric film temperature

This section describes the calculation of amplitude of temperature change induced by resistive heating of the gold strip and variation of film temperature with time. For pyroelectric characterization of the $BaTiO_3$ film, we estimated the amplitude of sinusoidal temperature oscillation using a one-dimensional heat diffusion equation in radial coordinates. The gold strip is modeled as a line-source of heat carrying electrical current at frequency ω, over a semi-infinite volume. This current causes a temperature oscillation in the sample at a frequency 2ω due to resistive heating of the metal strip. The frequency-dependent temperature oscillation amplitude of the semi-infinite substrate due to the line heat source of width $2b$ and length l is given by[31]

$$\Delta T_s = \frac{P}{l\pi\Lambda_s}\int_0^\infty \frac{\sin^2(kb)}{(kb)^2(k^2+q^2)^{1/2}}dk, \tag{1}$$

where $q^{-1}=(D/j2\omega)^{1/2}$ is the thermal penetration depth, $j=\sqrt{-1}$, P is the input electrical power, D is the substrate thermal diffusivity, and Λ_s is the substrate thermal conductivity. The thin films between the metal strip and substrate each add a frequency-independent temperature oscillation given by[32]

$$\Delta T_f = \frac{P}{l\Lambda_f}\frac{t}{2b}, \tag{2}$$

where t is the film thickness and Λ_f is the film thermal conductivity. The temperature oscillation amplitude of the $BaTiO_3$ film, calculated at the mid-point of the pyroelectric film thickness, is given by $\Delta T=\Delta T_s+\Delta T_{f,SrRuO3}+{}^1/_2\,\Delta T_{f,BaTiO3}$.[32] The contribution to ΔT from thin films was significantly smaller than the substrate contribution since the

TABLE I. Material properties used for thermal modeling.

	Thermal conductivity (W/m K)	Heat capacity (J/m^3 K)
PEVCD SiO_2	1.1	…
$BaTiO_3$	4.8	…
$SrRuO_3$	3	…
$GdScO_3$	2.4	2.7×10^6

films were only ~100 nm thick. Table I shows the thermal property values used for these calculations.[33] The 3ω method was used to measure the room temperature thermal conductivity of the $GdScO_3$ substrate.[31] The volumetric heat capacity of the substrate was assumed equal to that of the $SrTiO_3$ single crystalline substrate, whose crystal structure and density are similar to that of $GdScO_3$.[34] The error in the ΔT calculation due to the SiO_2 layer sandwiched between the $BaTiO_3$ film and gold heater was estimated to be <4%, and the error in the ΔT calculation due to the interfacial thermal resistance (assumed 2×10^{-8} m^{2}K/W)[35] was estimated to be <1%.

We measured the change in $BaTiO_3$ film temperature with time using the temporal pyroelectric response of the film under no applied bias. Figure 3 shows ΔT profiles for different heating voltage waveforms presented in this paper. The pyroelectric current from the $BaTiO_3$ film was measured from the bottom $SrRuO_3$ electrode, while the top $SrRuO_3$ electrode was grounded. The pyroelectric current depends upon the rate of change of temperature with time (t) and is given by $i_p = pA(dT/dt)$, where p is the pyroelectric coefficient and A is the area of the capacitor. We used a constant $p = -20\ \mu$C/m^{2}K to evaluate the average $\Delta T(t)$ of the pyroelectric film by integrating i_p with respect to time. The magnitude of ΔT thus obtained was implicitly calculated from the heat diffusion model described above; variation of ΔT in time was measured from the pyroelectric response of the thin film.

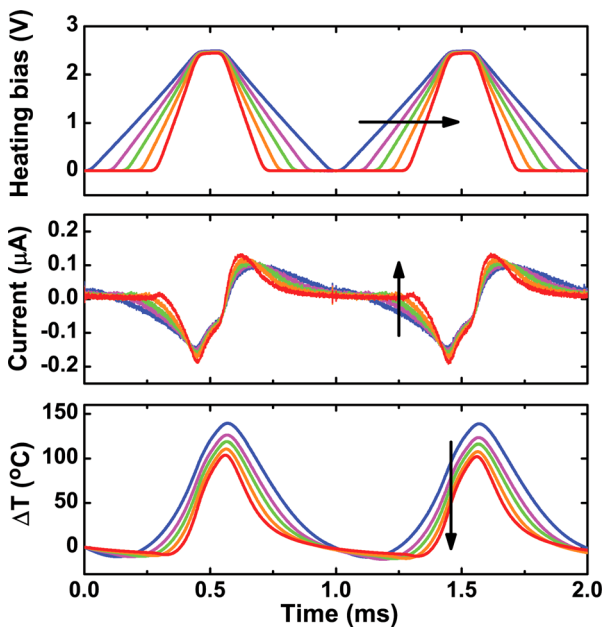

FIG. 3. Measured pyroelectric current and estimated temperature rise for different heating voltage profiles. The arrows point toward data with increasing heating rates.

III. RESULTS AND DISCUSSION

We used the microfabricated platform to control the temperature and electric field, and monitored the energy conversion cycles by measuring the displacement changes induced due to the pyroelectric and dielectric response of the $BaTiO_3$ thin film. All measurements reported in this section were done at a background temperature of 20 °C and the cycle frequency was 1 kHz. Results presented here show how the rates of temperature change, electric field switching and phase lag between thermal and electrical cycles affect the electrical energy density. The phase shift between ΔT and ΔE waveforms determines the film displacement at which the isothermal process ends and isoelectric process begins. Different temperature and electric field change rates, on the other hand, lead to processes that are no longer isothermal or isoelectric. In addition, varying ΔT and ΔE rates also influences the heat transfer through the sample and dielectric response of the pyroelectric film which affects energy conversion.

A. ΔT-ΔE phase difference

Energy conversion using pyroelectric cycles depends upon the synchrony between thermal and electrical cycles. Figure 4 shows the time-varying heating voltage, temperature change of the $BaTiO_3$ film, three phase-shifted out-of-plane electric field profiles, measured electric current, and the resulting film electric displacement change. In a traditional pyroelectric Ericsson cycle, the electric field switches at the maximum and minimum temperatures to obtain the highest electric displacement change and energy density. The temperature is held constant while the electric field changes. In the measurements shown in Figure 4, identical heating bias waveforms were used to obtain the same ΔT variation in the pyroelectric film with time. The electric field switches between 200 and 183 kV/cm at a 5.67×10^5 kV/cm-s ramp rate. The high electric field ramp rate ensures that the temperature is nearly constant. However, unlike the Ericsson cycle, the electric field does not necessarily switch at the highest and lowest temperatures, and depends on the phase of the electric field profile relative to the heating bias profile. Results are shown for phase angles −42°, 0°, and 42°, where zero phase corresponds to the case when the electric field switches at the mid-point of the heating bias maxima and minima. For −42° phase angle, the electric field switches (at $t = 0.1$ ms) before the corresponding temperature extreme is reached. The 0° electric field profile switches at the heating bias extremes which do not coincide with the temperature extremes as shown by the ΔT profile. For the profile with 42° phase angle, the electric field changes from high to low (at $t = 0.3$ ms) near the maximum temperature and from low to high (at $t = 0.8$ ms) before the minimum temperature is reached.

Different thermal-electrical cycles shown in Figure 5(a) for different phase angles are a result of staggered electric field waveforms, and dissimilar heating and cooling profiles.

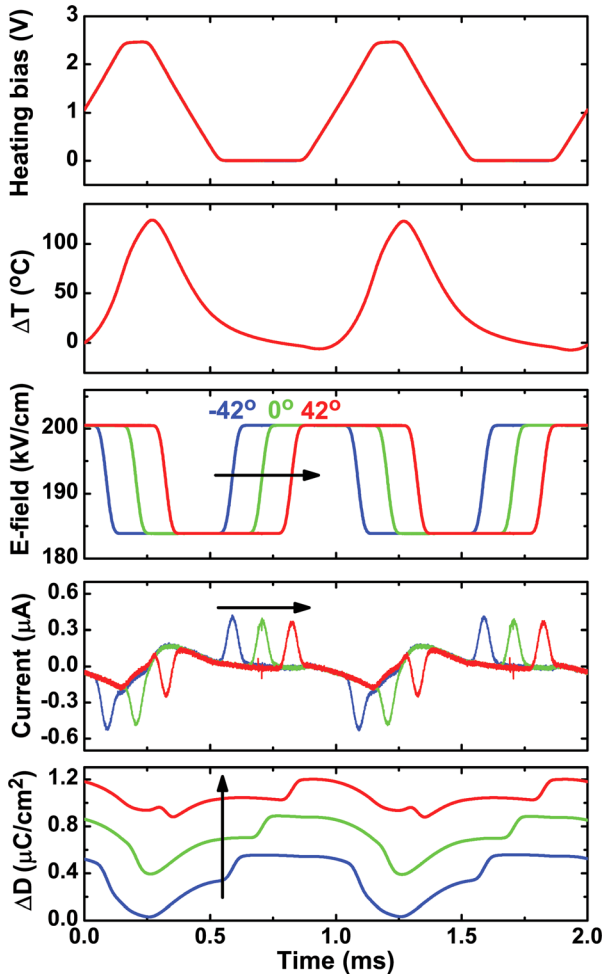

FIG. 4. Applied heating bias, estimated temperature change, out-of-plane electric field, measured current and electric displacement change versus time for electric field switching at phase angles −42°, 0°, and 42°. Zero-phase corresponds to the case when electric field switches at the mid-point of the heating bias extrema. A vertical offset is added to the ΔD plots for clarity. The arrows point toward data corresponding to increasing E-field switching phase.

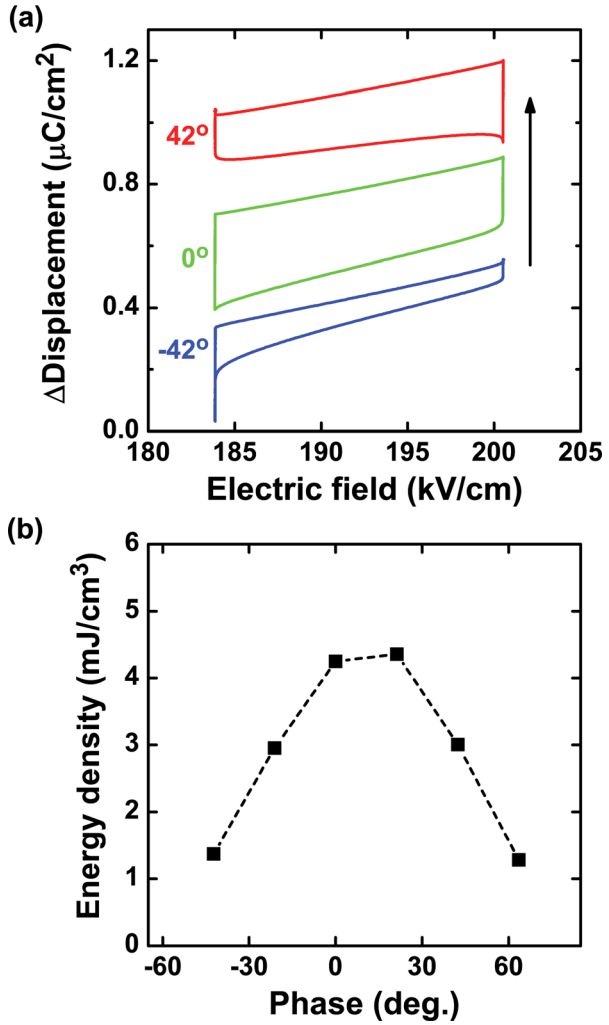

FIG. 5. (a) Pyroelectric Ericsson cycles shown on a *D-E* plot. The arrow shows increasing electric field switching phase. Cycles are shown with a vertical offset for clarity. (b) Measured energy density as a function of electric field switching phase.

For negative phase angles (shown in blue), the temperature first increases and then decreases at constant low electric field which results in a corresponding decrease followed by an increase in the electric displacement that does not contribute to electrical work out. Maximum electrical energy might be expected for the case when the electric field switches near the highest and lowest temperatures, as is the case for electric field profile phase-shifted by 42° (shown in red). Instead, the maximum energy density is observed for phase angles 0° or 21°, as shown in Figure 5(b), where the electric field decreases before the maximum temperature is reached. This counterintuitive result is a consequence of the competition between decrease in displacement due to a decrease in electric field and increase in displacement as the temperature decreases for the 42° phase profile. The finite dielectric response time, which depends on the electric field ramp rate, causes the field-driven reduction in displacement to coincide with the counteracting pyroelectric response during the initial cooling phase during which the temperature decreases at the fastest rate and the pyroelectric contribution to electric displacement is highest.

B. Electric field ramp rate

The electric field ramp rates determine the change in film temperature while the electric field varies since the temperature of the pyroelectric film changes continuously in our setup. Electric field switches nearly instantaneously at high ramp rates and the process is nearly isothermal, but the temperature-change-driven pyroelectric contribution can be significant for low electric field change rates when the processes are no longer isothermal. Figure 6 shows the time-varying heating voltage, estimated ΔT, applied electric field with different ramp rates, measured electric current, and the resulting film displacement change. The electric field transitions from high to low at the mid-point of the heating bias maxima corresponding to 0° phase angle for all measurements. The ΔD increase due to a rise in electric field (at $t = 0.7$ ms) is about the same for all cases but the decrease in ΔD (at $t = 1.2$ ms) is different for different ramp rates. While the dielectric contribution to the displacement change is about the same for an increase or decrease in electric field, the pyroelectric contribution changes depending on the rate of change of temperature. When the electric field increases,

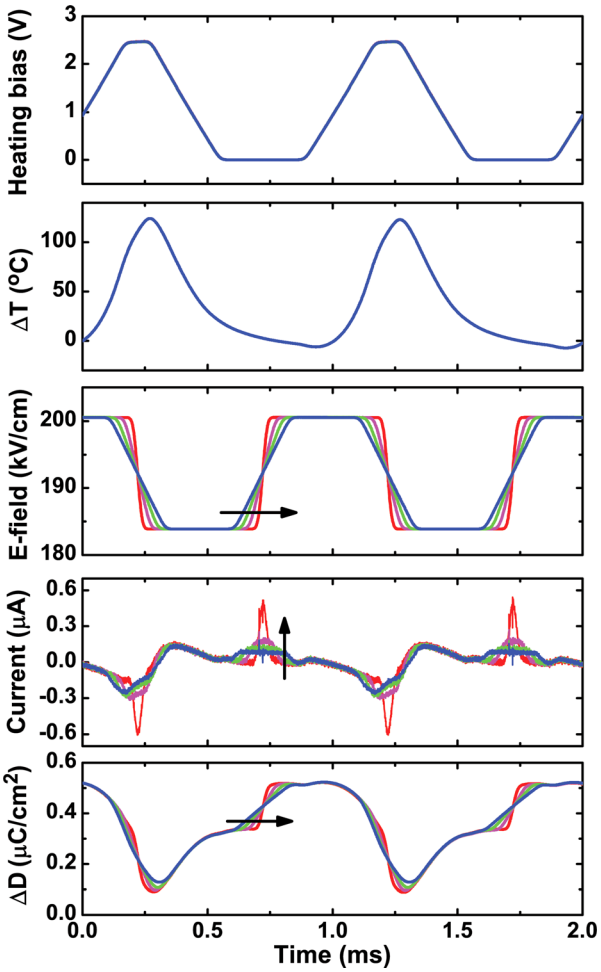

FIG. 6. (a) Applied heating bias, estimated temperature change, out-of-plane electric field, measured current and electric displacement change versus time for electric field change rates of 1.42×10^5, 2.83×10^5, 5.67×10^5, and 11.33×10^5 kV/cm-s. The arrows point toward data with increasing electric field ramp rates.

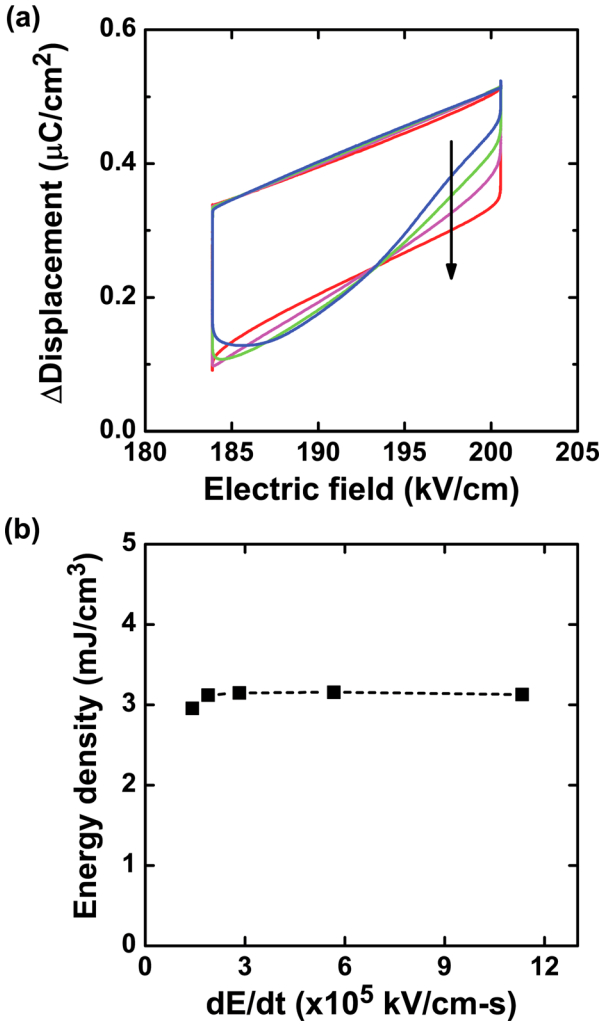

FIG. 7. (a) Pyroelectric Ericsson cycles shown on a *D-E* plot with increasing electric field ramp rates (represented by the direction of the arrow). (b) Measured energy density plotted as a function of electric field change rate.

the temperature is decaying slowly as heat is lost to the environment and the pyroelectric contribution is negligible. But when the electric field decreases, the temperature is increasing rapidly with the rising heating power, producing a significant pyroelectric-effect-induced displacement change.

Figure 7 shows the thermal-electrical cycles and measured energy densities for different electric field ramp rates. The isothermal condition is valid for the low temperature top branch of the clockwise cycles as the electric field increases from 183 kV/cm to 200 kV/cm irrespective of the electric field change rate since the accompanying reduction in film temperature is not significant. But the duration over which electric field decreases affects the bottom branch of the cycles as the temperature is changing simultaneously. For the slowest rate of 1.42×10^5 kV/cm-s (shown in blue), a decrease in electric field is initially accompanied by a rapid increase in temperature which results in a sharp drop in the electric displacement near 200 kV/cm. However as the electric field approaches 183 kV/cm, the temperature begins to decrease which increases the electric displacement. The temperature-driven increase in ΔD counteracts the field-driven decrease in electric displacement that eventually increases the total ΔD. The overall energy density, however, is nearly independent of the field change rate since the total temperature change is the same resulting in an identical pyroelectric response superimposed over the dielectric response which does not produce any electrical work by itself.

C. Temperature change ramp rate

We controlled the duration and rate of heating and cooling of the $BaTiO_3$ film by changing the slope of the heating bias versus time. Figure 8 shows five heating voltage profiles with different ramp rates, corresponding ΔT, applied electric field, measured electric current, and resulting film electric displacement change. The heating bias was increased linearly from 0 V to 2.5 V at varying rates, held constant at 2.5 V for 0.12 ms, and then decreased to 0 V. There is no temperature change when the voltage along the length of gold heater strip is zero. As the heating voltage V increases linearly, the temperature increases in proportion with the input heating power which scales as V^2. The temperature continues to increase when the heating bias is held constant due to the sample heat capacity. The maximum temperature is reached just as heating voltage begins to decrease (at $t = 0.6$ ms).

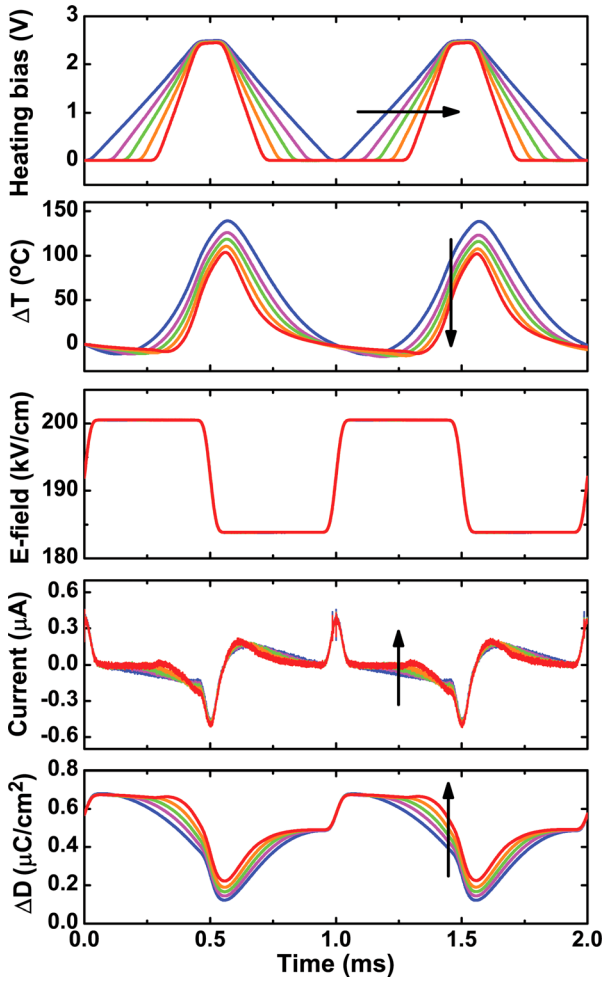

FIG. 8. (a) Applied heating bias, estimated temperature change, out-of-plane electric field, measured current and electric displacement change versus time for temperature change rates of 4.99×10^5, 5.36×10^5, 5.76×10^5, 6.27×10^5, and 7.06×10^5 K/s. The arrows point toward data with increasing heating rates.

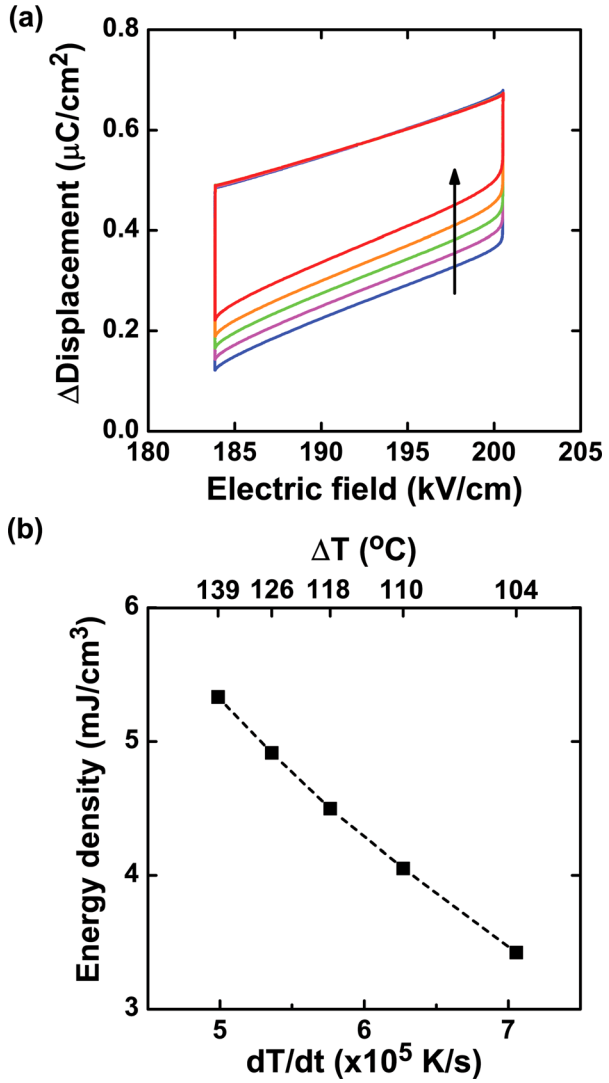

FIG. 9. (a) Pyroelectric Ericsson cycles shown on a *D-E* plot with increasing heating rates (represented by the direction of the arrow). (b) Measured energy density plotted as a function of average temperature change rate and the corresponding ΔT.

Thereafter, the sample is convectively cooled but the cooling rate is less than the heating rate and is dependent on the rate of heat transfer to the environment. A steeper heating voltage profile corresponds to a shorter heating period which results in a lower average temperature of the film due to non-uniform heating.[24] The electric field changes isothermally since the ramp rate is quite high at 5.67×10^5 kV/cm-s, and with phase angle of 0° relative to the heating bias. The displacement change due to a change in electric field is about the same for all heating profiles, but higher heating bias ramp rates result in smaller ΔD due to lower ΔT amplitudes as it decreases the pyroelectric contribution.

Figure 9 shows the thermal-electrical cycles and corresponding energy densities for different heating voltage ramp rates. The average temperature change ramp rate was calculated for each heating profile by dividing the maximum ΔT with the duration of temperature increase. Steeper heating voltage profiles resulted in lower ΔT which reduced the magnitude of displacement change due to the pyroelectric effect but did not alter the temperature change rates significantly. The lower average film ΔT reduced the total displacement change and electrical energy density. We also tried to achieve the same ΔT for the five heating voltage profiles shown here by varying the maximum applied heating bias to the extent possible, but did not observe any noticeable temperature-change-rate dependence of the output electrical energy density. This observation is consistent with previous studies which reported no significant dependence of the pyroelectric coefficient on the heating frequency.[30] While we did not observe a dependence of output energy density on the temperature-change-rate itself, we did notice the effect of heat transfer rate on ΔT and the generated electrical energy. These results highlight the importance of using thin films with small thermal mass and its placement near the heat source with rapid temperature fluctuations. In addition, design of the energy conversion platform should enhance conduction heat transfer within the platform as well as rapid convective cooling from the environment.

IV. CONCLUSION

In summary, we investigated the effect of temporal variations in temperature and electric field on pyroelectric

energy conversion using a microfabricated platform consisting of a 150 nm thick $BaTiO_3$ film. The platform allowed microsecond control of the temperature and electric field which enabled thermal-electrical cycles at a 1 kHz frequency. With the temperature and electric field profiles for the pyroelectric Ericsson cycle as the starting point, we studied the effect of three parameters: (1) the phase between ΔT and ΔE waveforms, (2) ΔE change rate, and (3) ΔT change rate. Maximum energy density was obtained when the electric field is switched from its maximum to minimum value before the highest temperature is reached rather than exactly at the ΔT maxima owing to the finite response time of the dielectric material. The electric field and ΔT change rates had no direct effect on the energy density, but higher ΔT change rates cause non-uniform heating of the pyroelectric film which reduced the measured energy density. We measured an energy density of around 3 mJ/cm^3 and power density of 3 W/cm^3 at representative electric field change rate of 5.67×10^5 kV/cm-s and ΔT change rate of 6.27×10^5 K/s from the $BaTiO_3$ films.

This work represents a significant improvement over earlier studies that were typically limited to pyroelectric cycles at frequencies less than 1 Hz due to a lack of precise electro-thermal control and large thermal mass of the pyroelectric materials used. Using the approach outlined in this paper, it should be possible to replicate temperature variations in real-world systems and design thermal-electrical cycles to maximize electrical energy output. The results presented provide a framework for optimizing the energy conversion performance of pyroelectric cycles in systems with high frequency temperature fluctuations, such as internal combustion engines and power electronics. We hope that this work will enable the use of pyroelectric materials for future waste heat harvesting applications.

ACKNOWLEDGMENTS

The authors gratefully acknowledge the support of ONR N00014-10-1-0525. A.R.D. gratefully acknowledges the support of ARO W911NF-10-1-0482.

[1]Lawrence Livermore National Laboratory. Energy International.
[2]G. J. Snyder and E. S. Toberer, Nature Mater. **7**, 105 (2008).
[3]C. B. Vining, Nature Mater. **8**, 83 (2009).
[4]D. G. Thombare and S. K. Verma, Renewable Sustainable Energy Rev. **12**, 1 (2008).
[5]M. E. Lines and A. M. Glass, *Principles and Applications of Ferroelectrics and Related Materials* (Clarendon Press, Oxford, 1977).
[6]Y. Yang, J. H. Jung, B. K. Yun, F. Zhang, K. C. Pradel, W. Guo, and Z. L. Wang, Adv. Mater. **24**, 5357 (2012).
[7]Y. Yang, W. Guo, K. C. Pradel, G. Zhu, Y. Zhou, Y. Zhang, Y. Hu, L. Lin, and Z. L. Wang, Nano Lett. **12**, 2833 (2012).
[8]Y. Yang, H. Zhang, G. Zhu, S. Lee, Z.-H. Lin, and Z. L. Wang, ACS Nano **7**, 785 (2013).
[9]E. Fatuzzo, H. Kiess, and R. Nitsche, J. Appl. Phys. **37**, 510 (1966).
[10]A. van der Ziel, J. Appl. Phys. **45**, 4128 (1974).
[11]R. B. Olsen, D. A. Bruno, and J. M. Briscoe, J. Appl. Phys. **58**, 4709 (1985).
[12]G. Sebald, S. Pruvost, and D. Guyomar, Smart Mater. Struct. **17**, 015012 (2008).
[13]H. Nguyen, A. Navid, and L. Pilon, Appl. Therm. Eng. **30**, 2127 (2010).
[14]C. D. Rakopoulos, K. A. Antonopoulos, D. C. Rakopoulos, and E. G. Giakoumis, Int. J. Energy Res. **28**, 977 (2004).
[15]W. E. Newell, IEEE Trans. Ind. Appl. **IA-12**, 405 (1976).
[16]L. Kouchachvili and M. Ikura, Int. J. Energy Res. **32**, 328 (2008).
[17]H. Y. Zhu, S. Pruvost, D. Guyomar, and A. Khodayari, J. Appl. Phys. **106**, 124102 (2009).
[18]R. Kandilian, A. Navid, and L. Pilon, Smart Mater. Struct. **20**, 055020 (2011).
[19]A. Khodayari, S. Pruvost, G. Sebald, D. Guyomar, and S. Mohammadi, IEEE Trans. Ultrason. Ferroelectr. Freq. Control **56**, 693 (2009).
[20]F. Y. Lee, A. Navid, and L. Pilon, Appl. Therm. Eng. **37**, 30 (2012).
[21]G. Cha and Y. S. Ju, Sens. Actuators, A **189**, 100 (2013).
[22]M. Ikura, Ferroelectrics **267**, 403 (2002).
[23]G. Sebald, E. Lefeuvre, and D. Guyomar, IEEE Trans. Ultrason. Ferroelectr. Freq. Control **55**, 538 (2008).
[24]B. Bhatia, "Nanometer-thick oxide films for pyroelectric energy conversion," Ph.D. Disseration (University of Illinois Urbana-Champaign, 2014).
[25]A. R. Damodaran, E. Breckenfeld, Z. Chen, S. Lee, and L. W. Martin, Adv. Mater. **26**(36), 6341–6347 (2014).
[26]K. J. Choi, M. Biegalski, Y. L. Li, A. Sharan, J. Schubert, R. Uecker, P. Reiche, Y. B. Chen, X. Q. Pan, V. Gopalan, L. Q. Chen, D. G. Schlom, and C. B. Eom, Science **306**, 1005 (2004).
[27]See supplementary material at http://dx.doi.org/10.1063/1.4901993 for $BaTiO_3$ film deposition and characterization, dielectric constant measurement versus temperature, and *D-E* and pyroelectric measurements.
[28]J. Karthik, A. R. Damodaran, and L. W. Martin, Adv. Mater. **24**, 1610 (2012).
[29]A. M. Glazer, P. Groves, and D. T. Smith, J. Phys. E: Sci. Instrum. **17**, 95 (1984).
[30]B. Bhatia, J. Karthik, T. Tong, D. G. Cahill, L. W. Martin, and W. P. King, J. Appl. Phys. **112**, 104106 (2012).
[31]D. G. Cahill, Rev. Sci. Instrum. **61**, 802 (1990).
[32]D. G. Cahill, M. Katiyar, and J. R. Abelson, Phys. Rev. B **50**, 6077 (1994).
[33]S. T. Davitadze, S. N. Kravchun, B. A. Strukov, B. M. Goltzman, V. V. Lemanov, and S. G. Shulman, Appl. Phys. Lett. **80**, 1631 (2002).
[34]Y. S. Touloukian and E. H. Buyco, *Thermophysical Properties of Matter* (IFI/Plenum, New York, 1970).
[35]S. M. Lee and D. G. Cahill, J. Appl. Phys. **81**, 2590 (1997).